



Pulsar Population Synthesis with Magnetorotational Evolution: Constraining the Decay of the Magnetic Field

Zhihong Shi and C.-Y. Ng

Department of Physics, The University of Hong Kong, Pokfulam Rd., Hong Kong, People's Republic of China

Received 2024 March 25; revised 2024 May 21; accepted 2024 May 27; published 2024 August 26

Abstract

We present a population synthesis model for normal radio pulsars in the Galaxy incorporating the latest developments in the field and the magnetorotational evolution processes. Our model considers spin-down with a force-free magnetosphere and the decay of the magnetic field strength and its inclination angle. The simulated pulsar population is fit to a large observation sample that covers the majority of radio surveys using the Markov Chain Monte Carlo technique. We compare the distributions of four major observables—spin period (P), spin-down rate (\dot{P}), dispersion measure, and radio flux density—using accurate high-dimensional Kolmogorov–Smirnov statistics. We test two B -field decay scenarios, an exponential model motivated by ohmic dissipation and a power-law model motivated by the Hall effect. The former clearly provides a better fit, and it can successfully reproduce the observed pulsar distributions with a decay timescale of $8.3^{+3.9}_{-3.0}$ Myr. The result suggests that significant B -field decay in aged pulsars and ohmic dissipation could be the dominant process.

Unified Astronomy Thesaurus concepts: Neutron stars (1108); Pulsars (1306); Radio pulsars (1353)

1. Introduction

The first pulsar was detected in 1967 (Hewish et al. 1969), and to date, there are over 3000 known pulsars in the sky according to the Australia Telescope National Facility (ATNF) catalog (Manchester et al. 2005). They are very interesting objects and powerful tools for probing many different aspects of physics, from relativity to gravity. For example, understanding their initial spin period (P_0) and magnetic field (B_0) distributions could reveal the angular momentum transport process and the origin of the B -field during core collapse. Modeling the pulsar population could provide tests of the emission mechanisms and constrain the event rates for the related high-energy astrophysical phenomena, including supernovae, fast radio bursts, gravitational waves, and gamma-ray bursts.

Normal pulsars lose their rotational energy in the form of particle wind and electromagnetic radiation, which results in spin-down. The spin parameters (P and \dot{P}) thus depend on the B -field strength and configuration. The evolution of the magnetic field could leave observable signatures on the pulsar rotational properties. This is the so-called magnetorotational evolution scenario (see Gullón et al. 2014).

That being said, the detailed evolution of the pulsar B -field remains an open question. There is indirect evidence that suggests magnetic field decay during the pulsar lifetime. For instance, the strongest B -fields are found in young pulsars and weak fields are found in old millisecond pulsars (MSPs), which is generally consistent with the idea of field decay expected from theories (e.g., Goldreich & Reisenegger 1992; Igoshev et al. 2021). Moreover, some pulsars are found to have a braking index deviated from 3, which could be the result of decreasing magnetic field strength (e.g., Viganò et al. 2013; Igoshev 2019) due to ohmic or Hall effects (Flowers &

Ruderman 1977; Goldreich & Reisenegger 1992; Igoshev & Popov 2015; Igoshev 2019) or evolution of the magnetic alignment angle (e.g., Weltevrede & Johnston 2008) by the plasma effect (Philippov et al. 2014).

Different theories suggest a wide range of decay timescales from a few 10^5 yr (Igoshev & Popov 2015) to 150 Myr (Bransgrove et al. 2018). Observationally, while the decay rate is difficult to measure directly, there are previous attempts to obtain constraints from population modeling. Most of the reported values are in the range of a few Myr (e.g., Gonthier et al. 2004; Cieřlar et al. 2020), but some found no evidence of decay (e.g., Faucher-Giguere & Kaspi 2006). In this study, we revisit this problem by developing a state-of-the-art population model that includes the latest developments in the field as realistic physics inputs and fit it to a large pulsar sample to constrain the model parameters. Our model adopts the spin-down formula in a plasma-filled magnetosphere (Spitkovsky 2006; Philippov et al. 2014) with the explicit dependence of α , the updated kick velocity distribution (Verbunt et al. 2017; Igoshev 2020), a sophisticated radio beam model (Gonthier et al. 2018), an updated free electron density distribution of the Galaxy (Yao et al. 2017), and the latest gamma-ray luminosity law and beam geometry (Watters et al. 2009; Kalapotharakos et al. 2017, 2019, 2022). In previous works, model comparison is often limited to pulsars from the Parkes and Swinburne Multibeam surveys (Edwards et al. 2001; Manchester et al. 2001) and the High Time Resolution Universe (HTRU) survey (Keith et al. 2010). We attempt to fit to a much larger observation sample that covers all major normal radio surveys. Finally, we employ, for the first time, a correct formula for the Kolmogorov–Smirnov (KS) statistic at high dimension for model comparison (Fasano & Franceschini 1987; Justel et al. 1997).

This paper is organized as follows. In Section 2, we introduce the simulation methods including five parts: birth properties, evolution, emission, detection, and comparison with observations. In Section 3, we report our simulation results for the optimal parameters and the corresponding population



Original content from this work may be used under the terms of the [Creative Commons Attribution 4.0 licence](https://creativecommons.org/licenses/by/4.0/). Any further distribution of this work must maintain attribution to the author(s) and the title of the work, journal citation and DOI.

properties. The discussion is in Section 4, and the conclusion is drawn in Section 5.

2. Simulation Method

2.1. Overview of the Simulation and Fitting Procedure

We adopt the evolution approach for the population synthesis. We follow the basic procedures outlined in Faucher-Giguere & Kaspi (2006) but with more realistic physics and model inputs from recent studies. First, we assign birth properties to newborn pulsars, i.e., P_0 , B_0 , α , location, kick velocity and direction, and viewing angle. Then each pulsar starts two independent evolution processes: magnetorotational evolution and dynamical motion under the Galactic gravitational potential. The evolution time of each pulsar is randomly assigned from a uniform distribution between 0 and 100 Myr. Since it is computationally more intensive to trace the pulsar motion in the Galaxy, we first calculate the evolution of P , \dot{P} , and α and use the final values to determine if a pulsar is visible. We assume a distance of 1 pc and set a threshold of 10^{-6} mJy MHz, which is much lower than the sensitivity of any radio surveys used in this study. If a pulsar is beamed away from the Earth or has radio flux below the above limit, we can safely assume that it cannot be detected and move on to simulate another pulsar. We calculate the orbits only for pulsars that pass this initial screening. We stress that this procedure has no effect on the simulated pulsar population since the two evolutions are independent. At the end of the simulation, we model the radio and gamma-ray emission based on their final spin property, location, and viewing geometry. A pulsar is only counted if it is detectable by the radio surveys in our list.

In each simulation run, we generate 10 times more detectable pulsars than the observation sample (i.e., a total of 18,590 pulsars). This number was chosen to minimize the statistical fluctuation while keeping the simulation efficient. See Appendix B for more details. After each run, we then determine the goodness of fit for a given set of model parameters by comparing the simulated pulsar distribution with the observations using a high-dimensional KS statistic. Finally, based on the KS statistic, we fit the model parameters using the Markov Chain Monte Carlo (MCMC) technique.

2.2. Birth Properties

2.2.1. Spatial Distribution

Normal pulsars are believed to be born in core-collapse supernovae of massive stars. Due to the short lifetime of the massive stars, the progenitors are not expected to travel far from their birthplace. We can therefore assume that pulsars are born very close to the spiral arms of the Galaxy. We adopt a logarithmic function to depict the four spiral arms of the Milky Way,

$$\theta(r_{xy}) = k \ln(r_{xy}/r_0) + \theta_0, \quad (1)$$

where k and θ_0 are constants from Wainscoat et al. (1992), $r_{xy} = \sqrt{x^2 + y^2}$, $\theta = \arctan(y/x)$, and x , y , z are coordinate values in a left-handed Galactocentric Cartesian coordinate system such that the Sun locates at $(x, y, z) = (8.5, 0, 0.025)$ kpc. We then adopt the radial distribution model of surface density

($\rho(r_{xy})$) for newborn pulsars,

$$\rho(r_{xy}) \propto r_{xy} \left(\frac{r_{xy} + R_l}{R_\odot + R_l} \right)^a \exp \left[-b \left(\frac{r_{xy} - R_\odot}{R_\odot + R_l} \right) \right], \quad (2)$$

where R_\odot is the distance from the Sun to the Galactic center and a , b , and R_l are constants from Yusifov & Küçük (2004). Next, we apply a polar angle correction θ_{corr} and distance adjustment r_{corr} to each pulsar following Faucher-Giguere & Kaspi (2006) to blur the pulsar distribution so that they are not all piled up at the centroids of arms. Finally, a two-sided exponential function is applied to describe the distribution of vertical distance above and below the Galactic plane with a scale height z_0 of 50 pc:

$$\rho(z) = \frac{1}{2z_0} \exp \left(-\frac{|z|}{z_0} \right). \quad (3)$$

2.2.2. Kick Velocity

Much direct observational evidence supports the idea that neutron stars receive natal kicks during supernova explosions. For instance, young pulsars can reach a velocity range from tens to over 1000 km s^{-1} , while their progenitors, i.e., O-B stars, have a low velocity of only $\sim 10\text{--}30 \text{ km s}^{-1}$. Moreover, the scale height of the spatial distribution of pulsars in the Galaxy is ~ 300 pc (Lorimer et al. 2006), significantly larger than that of the progenitors (~ 50 pc). Previous studies tried different ways to parameterize the velocity distribution, including bimodal (Arzoumanian et al. 2002), single Maxwellian (Hobbs et al. 2005), and bimodal Maxwellian (Verbunt et al. 2017; Igoshev 2020). In our simulation, we adopt the two-component isotropic Maxwellian distribution suggested by a recent work (Igoshev 2020):

$$f_{\text{max}}(v|\sigma) = \sqrt{\frac{2}{\pi}} \frac{v^2}{\sigma^3} \exp \left(-\frac{v^2}{2\sigma^2} \right) dv \quad \text{and} \quad (4)$$

$$f(v|w, \sigma_1, \sigma_2) = w f_{\text{max}}(v|\sigma_1) + (1 - w) f_{\text{max}}(v|\sigma_2). \quad (5)$$

We fix $w = 0.2$, $\sigma_1 = 56 \text{ km s}^{-1}$, and $\sigma_2 = 336 \text{ km s}^{-1}$, obtained by fitting a sample of young pulsars with a characteristic age younger than 3 Myr old (Igoshev 2020). The velocity is assumed to have a random direction drawn from an isotropic distribution.

Note that we do not attempt to fit the pulsar spatial or velocity distributions, as they are insensitive to the magnetorotational evolution of pulsars, which is the focus of this work.

2.2.3. Initial Spin and Magnetic Field

We regard the initial period P_0 and magnetic field B_0 as independent from other properties, although they could be a potential connection (e.g., between P_0 and v ; see Ng & Romani 2007).

In the previous population synthesis study, the pulsar initial magnetic field strength B_0 and period P_0 are assumed to draw from lognormal distributions (e.g., Graber et al. 2024). This is supported by recent studies, which show that lognormal is preferred over normal distribution for both B_0 and P_0 (Igoshev et al. 2022; Xu et al. 2023).

This is adopted in our simulation,

$$p(\log P_0) = \frac{1}{\sqrt{2\pi\sigma_P^2}} \exp\left[-\frac{(\log P_0 - \mu_P)^2}{2\sigma_P^2}\right], \quad (6)$$

$$p(\log B_0) = \frac{1}{\sqrt{2\pi\sigma_B^2}} \exp\left[-\frac{(\log B_0 - \mu_B)^2}{2\sigma_B^2}\right], \quad (7)$$

where μ_P , σ_P , μ_B , and σ_B are free parameters determined by fitting.

Finally, for each simulated pulsar, we assigned a random initial inclination angle α (between the magnetic and rotational axes) and a random viewing angle ξ (between the spin axis and line of sight), both drawn from isotropic distribution in 3D, i.e., $\cos \alpha$, $\cos \xi \sim \text{uniform}(0, 1)$.

2.3. Pulsar Evolution

2.3.1. Magnetorotational Evolution

The spin-down process of pulsars converts their rotational kinetic energy into electromagnetic radiation and particle outflow, resulting in an increasing period at a rate of \dot{P} . For the simplest model of a rotating dipolar magnetic field in vacuum, \dot{P} is related to field strength B at the magnetic equator and the magnetic inclination angle α ,

$$B^2 = \frac{1}{\sin^2 \alpha} \frac{3Ic^3}{8\pi^2 R^6} P\dot{P}, \quad (8)$$

where I is the pulsar moment of inertia, c is the speed of light, and R is the pulsar radius. Taking the canonical values of $R = 10^6$ cm and $I = 10^{45}$ g cm² gives

$$B = 3.2 \times 10^{19} \sqrt{P\dot{P}/\sin^2 \alpha} \text{ G}. \quad (9)$$

This standard spin-down formula was commonly adopted in previous population synthesis studies (e.g., Faucher-Giguere & Kaspi 2006; Gonthier et al. 2007; Popov et al. 2010). Recent numerical simulations of the pulsar magnetosphere found a more realistic force-free spin-down model of

$$\dot{P} = \frac{4\pi^2 R^6 B^2}{Ic^3 P} (k_0 + k_1 \sin^2 \alpha), \quad (10)$$

i.e., $\sin^2 \alpha$ dependence becomes $(k_0 + k_1 \sin^2 \alpha)$, such that even an aligned rotator ($\alpha = 0$) can spin down (Spitkovsky 2006; Kalapotharakos & Contopoulos 2009; Pétri 2012; Tchekhovskoy et al. 2013; Philippov et al. 2014). During spin-down, the electromagnetic torque exerted by the plasma-filled magnetosphere also causes the magnetic axis to progressively align with the rotational axis (Beskin et al. 1988; Philippov et al. 2014; Igoshev & Popov 2020). We follow Philippov et al. (2014) to model this with

$$\dot{\alpha} = -\frac{4\pi^2 R^6 B^2}{Ic^3 P^2} k_2 \sin \alpha \cos \alpha, \quad (11)$$

where the numerical factors k_0 , k_1 , and k_2 have a weak dependence on the ratio between neutron star radius and light cylinder radius. For a typical pulsar, $k_0 \approx k_2 \approx 1.0$, $k_1 \approx 1.2$ (Philippov et al. 2014). As mentioned in the Introduction, there is observational evidence suggesting the decay of the pulsar's magnetic field over its lifetime. Taking this into account in the

population synthesis affects the evolution of \dot{P} and α , and hence the pulsar evolutionary tracks in the P – \dot{P} diagram. We consider in this work the B -field decay in the crust due to ohmic loss and the Hall effect. The decay in the core is ignored, since the core can be considered as a nearly neutral superconductor, which has a very long decay timescale. Ohmic decay is the result of scattering between phonons and impurities of the crystalline lattice (e.g., Pethick & Sahrhling 1995; Igoshev & Popov 2020). It can be parameterized by an exponential function,

$$B(t) = B_0 \exp\left(-\frac{t}{\tau_{\text{Ohm}}}\right), \quad (12)$$

where timescale τ_{Ohm} is related to the impurities, conductivity, and spatial scale of the crust (Igoshev et al. 2021). On the other hand, the Hall effect redistributes the magnetic energy, leading to nonlinear decay as

$$B(t) = \frac{B_0}{1 + t/\tau_{\text{Hall}}}, \quad (13)$$

with a timescale τ_{Hall} that depends on the initial magnetic field B_0 .

These two effects can be described by a more general form of B -field decay,

$$\frac{dB(t)}{dt} = -f_B B(t)^{1+\alpha_B}, \quad (14)$$

as suggested by numerical calculations (Colpi et al. 1999; Beniamini et al. 2019; Jawor & Tauris 2022). Here the power-law index α_B indicates the decay contribution of ohmic dissipation and the Hall effect. Integrating the equation above, the magnetic field evolution thus follows:

$$B(t) = \begin{cases} B_0 \exp(-f_B t) & \text{if } \alpha_B = 0 \\ B_0(1 + \alpha_B f_B B_0^{\alpha_B} t)^{-1/\alpha_B} & \text{if } \alpha_B > 0. \end{cases} \quad (15)$$

It is obvious that when $\alpha_B = 0$, the equation above reduces to Equation (12) with $\tau_{\text{Ohm}} = 1/f_B$. For the special case of $\alpha_B = 1$, it reduces to Equation (13) with $\tau_{\text{Hall}} = 1/B_0 f_B$. In our simulations, we implement the two functions in Equation (15) separately to avoid numerical instability when α_B is close to 0. We fit τ_{Ohm} for the exponential decay case and f_B and α_B for the power-law decay case. Finally, we also introduce a minimum magnetic field strength $B_{\text{min}} = 10^8$ G (Zhang & Kojima 2006) so that it does not decrease to unphysical values. We will show in Section 3 that our result is insensitive to B_{min} , since almost no pulsar B -fields can reach this limit at the end of the simulation.

At each time step of integration, the value of B is first calculated, then used to determine changes of P and α according to Equations (10) and (11). The simulation of each pulsar is terminated at a maximum age randomly chosen within 100 Myr.

2.3.2. Dynamical Evolution

After a pulsar is born, we trace its orbit in the Galactic gravitational potential during its lifetime as in previous studies (e.g., Cieřlar et al. 2020). The gravitational potential mainly consists of contributions from the Galactic disk, bulge, and

dark matter halo. We use the model given by Miyamoto & Nagai (1975) to characterize the gravitational potential of the bulge and the disk,

$$\Phi_{\text{bulge}} = -\frac{GM_b}{\sqrt{b_b^2 + R^2}}, \quad (16)$$

$$\Phi_{\text{disk}} = -\frac{GM_d}{\sqrt{(a_d + \sqrt{b_d^2 + z^2})^2 + r_{xy}^2}}, \quad (17)$$

respectively, where the bulge mass is $M_b = 1.12 \times 10^{10} M_\odot$ and the disk mass is $M_d = 8.78 \times 10^{10} M_\odot$, $b_b = 0.277$ kpc, $a_d = 4.2$ kpc, and $b_d = 0.198$ kpc. R and r_{xy} are the distance and radial distance to the Galactic center, respectively. For the halo potential, we follow the model by Paczynski (1990),

$$\Phi_{\text{halo}} = -\frac{GM_h}{2r_c} \left[\frac{2r_c}{R} \arctan\left(\frac{R}{r_c}\right) + \ln\left(1 + \frac{r_c^2}{R^2}\right) \right], \quad (18)$$

where the halo mass is $M_h = 5 \times 10^{10} M_\odot$ and $r_c = 6$ kpc. Since the mass of the halo is divergent, we applied a cutoff radius of $r_{\text{cut}} = 100$ kpc, beyond which the halo density drops to 0 and $\Phi_{\text{halo}} \propto r^{-1}$, following Belczynski et al. (2010).

2.4. Pulsar Emission

After the simulation, we calculate the radio and gamma-ray emission of a pulsar using its final properties (e.g., P , B , viewing angle, distance, dispersion measure (DM), etc.) to determine if they are detectable by the surveys.

2.4.1. Radio Emission

The observed pulsar radio emission geometry can be modeled by core and cone components (Rankin 1993). This empirical model has been widely used in previous population synthesis studies (e.g., Arzoumanian et al. 2002; Gonthier et al. 2004, 2018; Harding et al. 2007). In this work, we follow Gonthier et al. (2018) to describe the beam geometry and radio flux density S_ν .

First, we adopt an empirical power-law function to parameterize the total radio luminosity,

$$L_\nu = L_{\text{cone}} + L_{\text{core}} = f_\nu P^{\alpha_\nu} \dot{P}^{\beta_\nu}_{-21}, \quad (19)$$

where the total radio luminosity L_ν , the cone luminosity L_{cone} , and the core luminosity L_{core} are measured in mJy kpc² MHz; P_{-3} is the spin period in 10^{-3} s; \dot{P}_{-21} is the spin-down rate in 10^{-21} s s⁻¹; and f_ν , α_ν , and β_ν are free parameters determined by fitting. The ratio \mathcal{R} between the core and cone luminosities depends on P , \dot{P} with a broken power law,

$$\mathcal{R} = \begin{cases} 6.2 P \dot{P}_{-15}^{-0.07} & P < 0.7 \text{ s} \\ P^{-2.1} \dot{P}_{-15}^{-0.07} & P \geq 0.7 \text{ s}. \end{cases} \quad (20)$$

The simulated pulse profile of radio emission is axisymmetric and depends on the survey frequency ν and polar angle θ as

$$F(\nu, \theta) = F_{\text{core}} e^{-\theta^2/\rho_{\text{core}}^2} + F_{\text{cone}} e^{-(\theta-\bar{\theta})^2/w_e^2}, \quad (21)$$

where

$$F_i(\nu) = \frac{-1 + \alpha_i}{\nu} \left(\frac{\nu}{50 \text{ MHz}} \right)^{\alpha_i+1} \frac{L_i}{\Omega_i D^2}. \quad (22)$$

ρ_{core} and w_e are the effective width of the core and cone beam, and $\bar{\theta}$ is the hollow cone beam annulus size. The index i refers to the cone or core component. The spectral index α_i is given by Harding et al. (2007), and D is the distance in kpc. The polar angle θ is related to the magnetic inclination angle α , the viewing angle ξ , and the rotational phase ϕ by

$$\cos \theta = \sin \xi \sin \alpha \cos \phi + \cos \alpha \cos \xi. \quad (23)$$

The normalization factors are given by

$$\begin{aligned} \Omega_{\text{core}} &= \pi \rho_{\text{core}}^2, \\ \Omega_{\text{cone}} &= 2\pi^{3/2} \omega_e \bar{\theta}. \end{aligned} \quad (24)$$

The core beam is a Gaussian function that scales with spin period as

$$\rho_{\text{core}} = 1^\circ 5 P^{-0.5}. \quad (25)$$

The cone beam has a hollow Gaussian form with the annulus size and width as

$$\begin{aligned} \bar{\theta} &= (1 - 2.63 \delta_w) \rho_{\text{cone}}, \\ w_e &= \delta_w \rho_{\text{cone}}, \end{aligned} \quad (26)$$

respectively, where $\delta_w = 0.18$ (Gonthier et al. 2006) and the opening angle depends on the pulsar emission altitude r_{KG} and spin period P (Kijak & Gil 1998) as

$$\rho_{\text{cone}} = 1^\circ 24 r_{\text{KG}}^{0.5} P^{-0.5}, \quad (27)$$

with r_{KG} estimated using the pulse width method (Kijak & Gil 2003),

$$r_{\text{KG}} = 40 \dot{P}_{-15}^{0.07} P^{0.3} \nu_{\text{GHz}}^{-0.26}, \quad (28)$$

where ν_{GHz} is the observation frequency in GHz. Equation (22) shows how the radio flux density drops as the polar angle θ increases. Given ξ and α , the observed pulse intensity variation with the rotational phase ϕ can be calculated according to Equation (23). This gives the radio pulse profile. We then calculate the phase-averaged radio flux density to determine if the pulse is brighter than the minimum detectable threshold of different radio surveys.

We follow some previous work and do not assume a death line for the radio emission (e.g., Gullón et al. 2014; Graber et al. 2024), such that the intrinsic radio emission of old pulsars does not completely shut down. On the other hand, the assumed luminosity law (Equation (19)) will naturally make old pulsars become too faint to be detected.

2.4.2. Gamma-Ray Luminosity and Beaming Geometry

One of the applications of our population synthesis study is making predictions for the number of detectable gamma-ray pulsars. We model the gamma-ray luminosity with the fundamental plane relation (Kalapotharakos et al. 2022)

$$L_\gamma = 10^{14.3} \varepsilon_{\text{cut}}^{1.39} B_p^{0.12} \dot{E}^{0.39}, \quad (29)$$

where ε_{cut} is the cutoff energy in units of MeV obtained from the empirical $\varepsilon_{\text{cut}}-\dot{E}$ relations (Kalapotharakos et al. 2017); B_p is the field strength at the magnetic pole, i.e., twice the value of B in our simulation; and L_γ and \dot{E} are in units of erg s⁻¹. The

Table 1
Number of Normal Pulsars Detected from Radio Surveys Compared with Our Best-fit Model Simulation Results

Survey ^a	ar1	ar3	ar4	palfa	gb2	gb3	gbncc	htru_pks	mol2	pkshl	pks70	pkssw	pkmb	lotaas
Obs. no.	48	59	103	249	75	86	307	981	220	31	271	196	1016	257
Sim. no.	49	68	166	255	81	164	467	1226	256	31	204	195	729	310

Note.

^a See Table 6 in Appendix A for the full names of the surveys.

observed phase-averaged gamma-ray flux is given by

$$F_\gamma = \frac{L_\gamma}{4\pi f_\Omega D^2}, \quad (30)$$

where the beaming factor f_Ω depends on the viewing angle ξ , α , and gamma-ray efficiency ($w = \eta \propto \dot{E}^{1/2}$).

We adopt the results from the outer gap (OG) and two-pole caustic (TPC) models to estimate f_Ω (Watters et al. 2009). For the OG model,

$$f_\Omega \approx \begin{cases} 0.17 - 0.69w + (1.15 - 1.05w)(\alpha/90^\circ)^{1.9} & \xi < 60^\circ \\ 0.17 - 0.69w + (1.15 - 1.05w)(\alpha/90^\circ)^{1.9} \\ -1.35(2/3 - \xi/90^\circ) & \xi > 60^\circ. \end{cases} \quad (31)$$

For the TPC model,

$$f_\Omega \approx \begin{cases} 0.8 + 1.2(0.3 - w)\cos(2\beta) & \xi > \xi_I \\ 0.3 + 1.5(1 - w)[1 + (\xi - \xi_I)/90^\circ] & \xi < \xi_I, \end{cases} \quad (32)$$

where $\beta = \xi - \alpha$ and ξ_I relates to the boundary of the hollow cone above the null charge surface,

$$\xi_I = (75 + 100w) - (60 + 1/w)(\alpha/90^\circ)^{2(1-w)}. \quad (33)$$

We do not attempt to fit any of the parameters here due to the relatively small sample size of gamma-ray pulsars. Therefore, this has no impact on other parameters of our population model and B -field evolution.

2.5. Radio Detection

To determine the visibility of a simulated pulsar for a specific radio survey, we first check if the pulsar's final location lies inside the survey region. If so, we calculate the DM from its final location with the latest free electron density model of the Galaxy (Yao et al. 2017). Then we employ the standard radiometer formula (Dewey et al. 1985) to compare the pulsar flux density and the detection threshold S_{\min} of the survey,

$$S_{\min} = \frac{C\beta[T_{\text{rec}} + T_{\text{sky}}(l, b)]}{G\sqrt{N_p t_{\text{obs}} \Delta F}} \sqrt{\frac{W_e}{P - W_e}}, \quad (34)$$

where C is the detection signal-to-noise threshold, β is the degradation factor caused by system loss, T_{rec} is the receiver system temperature in K, $T_{\text{sky}}(l, b)$ is the sky background temperature in K obtained from the all-sky atlas (Haslam et al. 1982), G is the effective gain of the telescope antenna in units of K Jy^{-1} , N_p is the number of polarizations, t_{obs} is the observation time in s, ΔF is the total bandwidth in MHz, P is the pulsar period in s, and W_e is the effective pulse width in ms. We estimate W_e based on the formulae given by Bhat et al. (2004), and we follow previous studies (e.g., Lorimer et al.

1993; Bates et al. 2014) to estimate G from the original telescope gain G_0 by

$$G = G_0 \exp\left(\frac{-2.77r^2}{w^2}\right). \quad (35)$$

This accounts for the decrease in sensitivity when a pulsar has an offset r from the telescope pointing center. Here w is the full width at half-maximum (FWHM) of the telescope beam and r is randomly chosen assuming a uniform distribution of r^2 between 0 and $w^2/4$ (Bates et al. 2014).

If a simulated pulsar lies within the survey area with a radio flux density above the survey sensitivity, then it is considered as detected, and its parameters will be compared with the observed pulsar sample using the procedure described in Section 2.6 below. Regardless of whether a simulated pulsar is detected or not, it is always counted for the birth rate calculation.

2.6. Model Comparison and Parameter Optimization

2.6.1. Pulsar Sample

We select our pulsar sample from the major surveys listed in the ATNF catalog¹ (Manchester et al. 2005) with the following criteria.

1. $P > 0.03$ s and $\dot{P} > 0$ to rule out MSPs.
2. Exclude rotating radio transients and binary pulsars, as these could have different formation channels and evolution paths than normal pulsars.
3. Exclude radio surveys with fewer than 25 normal pulsars to speed up the computing time. These are listed in Table 5 in Appendix A. This leads to only 38 fewer pulsars, which is not significant.
4. Exclude surveys that are fully overlapped with others (see Table 5 in Appendix A).
5. Exclude ongoing surveys (e.g., the MeerKAT TRAPUM Survey).
6. Exclude 87 pulsars that have DM-estimated distances larger than 25 kpc, which are likely to be extragalactic.

The above selection criteria give a total of 1859 radio pulsars from 14 surveys covering the vast majority of normal radio pulsars. Table 1 shows the number of pulsars from each survey, and the survey parameters are presented in Table 6.

Our simulations assume that the radio flux density is measured at 1400 MHz (S_{1400}). However, there are 235 pulsars in our sample that only have measurements in other bands. We scale their flux densities to 1400 MHz assuming a typical spectral index of -1.60 (Jankowski et al. 2018). We show in Appendix A that this does not change the flux density distribution.

¹ <https://www.atnf.csiro.au/research/pulsar/psrcat/index.html>

2.6.2. Fitting of the Model Parameters

To evaluate the goodness of the model fit given a set of parameters, we compare the distribution of simulated and observed pulsar properties using a multivariate KS statistic (Fasano & Franceschini 1987; Justel et al. 1997). The procedure is outlined in Appendix B. We follow previous works (e.g., Gonthier et al. 2018) to focus on four observables, P , \dot{P} , DM, and S_{1400} , as other observables are not sensitive to the magnetorotational evolution model that we are interested in.

The fitting parameters are μ_P , σ_P , μ_B , σ_B , α_B , f_B , f_ν , α_ν , and β_ν for the power-law decay model. For the ohmic decay model, f_B is replaced with τ_{Ohm} , and there is one fewer free parameter as $\alpha_B = 0$. We employed the MCMC technique to search for the optimal model parameters. Given a KS statistic D_{KS} , the p -value can be calculated as

$$P(>Z) = 2 \sum_{k=1}^{\infty} (-1)^{k-1} e^{-2k^2 Z^2}$$

$$Z = \sqrt{\frac{n_1 n_2}{n_1 + n_2}} D_{\text{KS}}, \quad (36)$$

where n_1 and n_2 are the sample size of the simulation and observation (Fasano & Franceschini 1987). This is then used to construct the likelihood function in MCMC. There are no truncated values for the free parameters. We assume log-uniform priors for τ_{Ohm} , f_ν and uniform priors for all other fitting parameters and employed the `emcee` package (Foreman-Mackey et al. 2013) to run the MCMC chains.

3. Results

3.1. Best-fit Model Parameters

The best-fit power-law model suggests a very small value of α_B close to 0, which reduces the model to exponential decay. As we will show in Section 3.4 below, the model with large α_B produces pulsars narrowly distributed in P – \dot{P} space, which does not fit the observed pulsar population.

Figure 1 shows the corner plot for the exponential model parameters, obtained from MCMC with four independent chains of 16 walkers and 2500 steps each, a total of 160,000 simulations. The optimal parameters determined from the most probable values, i.e., at the maximum marginal probability density, with 68% confidence intervals, are listed in Table 2. As indicated in the figure, the model parameters μ_B , σ_B , τ_{Ohm} , and β_ν are well constrained, but f_ν , the lower bound of μ_P , and the upper bound of σ_P are not very well determined. In addition, there exist strong correlations between f_ν and α_ν and between μ_P and σ_P and some correlations among τ_{Ohm} , μ_B , α_ν , and β_ν .

3.2. Best-fit Pulsar Population

Table 1 shows a comparison between the observed and simulated number of pulsars in different surveys. The latter is obtained from the average of 100 simulations using the best-fit model parameter. These numbers are generally consistent and are very well matched for the palfa and pkshl surveys. However, some surveys, including ar4, gb3, and pksmb, show a significant discrepancy of up to 50%. The possible cause of this will be discussed in Section 4.4. In Figure 2, we compare the distributions of observables for the simulation and pulsar sample. We plot the four observables in the first row of Figure 2 (P , \dot{P} , DM, and S_{1400}) that are used to determine the

goodness of fit and also the pulsar Galactic coordinates, the B -field, and the characteristic age $\tau_c \equiv P/2\dot{P}$. The results show that our model can generally reproduce the observed pulsar population. The only exception may be the Galactic longitude, which has an obvious excess at $l \sim 30^\circ$ that our model fails to capture. This problem was first noted by Faucher-Giguere & Kaspi (2006) and is due to the spiral arm structure that cannot be accurately reproduced by the simple spatial model in Equation (1).

We also show in the figure a comparison between the true B -field in the simulation and the B -field estimated from spin-down using Equation (9) with $\sin \alpha = 1$, i.e.,

$$B_{\text{SD}} = 3.2 \times 10^{19} \sqrt{P\dot{P}} \text{ G}, \quad (37)$$

which is commonly adopted in the literature. They have very similar distributions, and the true B -field is slightly smaller. This is expected, as a direct comparison between Equations (10) and (37) gives $B/B_{\text{SD}} = \sqrt{3/(2 + 2.4 \sin^2 \alpha)}$, which varies between 0.55 and 0.82. In other words, Equation (37) is indeed a good approximation to the realistic force-free spin-down model. Finally, we show the age distribution of the simulated pulsars and its comparison with τ_c . The mean true age is 4.8 Myr, and over 40% of them are older than τ_{Ohm} . τ_c shows a good agreement with the true age for young pulsars up to ~ 1 Myr and then becomes much larger beyond that. This can be attributed to the decay of the B -field, which makes \dot{P} drop rapidly (see discussion in Section 3.4 below), thus resulting in large τ_c .

Figure 3 shows the P – \dot{P} diagram of the observed pulsar sample and a random realization of the best-fit model with the same number of pulsars. They generally show a good match. We notice that our model fails to reproduce pulsars in the lower left corner of the diagram (i.e., with fast spin but small \dot{P}). These could be mildly recycled pulsars, and their formation is not modeled in our simulation.

3.3. Dynamical Evolution

We plot in Figure 4 the location of the pulsar sample in Galactic coordinates and a Monte Carlo realization of our model for comparison. They show a good agreement in general. Results of the pulsar dynamical evolution are plotted in Figure 5. These include distributions of pulsar displacements and velocities. The pulsar displacement plot suggests that most pulsars do not travel far over their lifetime. Over 78% of them are found within 3 kpc of their birth site at the end of the simulation. Similarly, the velocity distribution plot shows that the final velocities (v_{final}) do not change much from the initial values (v_0). They follow the same double Maxwellian distribution with identical peak locations but slightly fewer ($\sim 1.3\%$ drop) pulsars in the low-velocity component ($< 130 \text{ km s}^{-1}$) and more ($\sim 1.1\%$ increase) with 200 – 300 km s^{-1} . All these results suggest that acceleration due to Galactic gravitational potential is not significant for most pulsars.

3.4. Magnetorotational Evolution

To investigate the effect of magnetic field decay on pulsar magnetorotational evolution, we plot in Figure 6 the pulsar evolutionary tracks in the P – \dot{P} diagram and the time evolution of B -field strength and inclination angle. These are calculated using the best-fit exponential decay model with $\tau_{\text{Ohm}} = 8.3 \text{ Myr}$. We

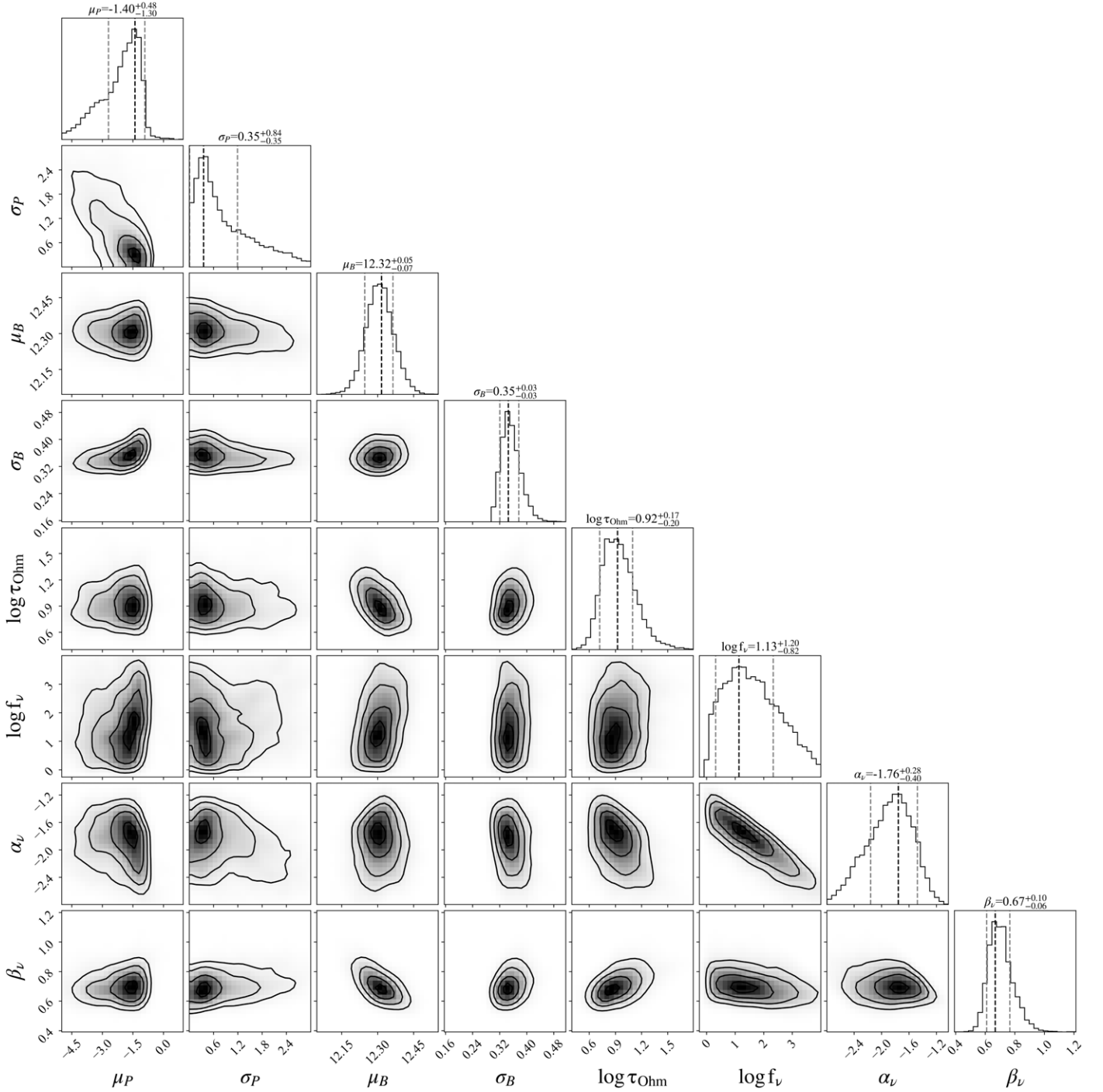


Figure 1. The MCMC marginal parameter space for the ohmic dissipation assumption. The 2D marginal plot is smoothed using a Gaussian kernel.

set $P_0 = 0.03$ s and initial $\alpha = 60^\circ$ and try different initial B -fields from $B_0 = 10^{11.5}$ G to $10^{13.5}$ G. For illustration purposes, we also plot the power-law decay model with $\alpha_B = 1.0$ and $\log f_B = -26.8$.

As shown in the top panels of the figure, the tracks in both scenarios show similar behavior at the beginning. They all follow straight lines of constant B -field, since the field decay is not significant at early times. For the exponential decay model, the tracks turn vertically downward when the pulsars are older than τ_{Ohm} , which is due to B -field decay, such that \dot{P} becomes very small ($\dot{P} \propto B^2$; see Equation (10)), and hence P stays nearly constant.

The power-law decay model shows a similar overall trend, but the detailed evolutionary tracks after the turning point depend on B_0 . The large B_0 tracks start to turn downward earlier. This is because the B -field decay timescale depends on $1/B_0$ according to Equation (15); i.e., a larger initial B -field decays faster. For this reason, all pulsars end up with similar B -fields around 10^{11} G at 100 Myr, much higher than that in the exponential model. This is clearly seen in the B -field evolution plot in Figure 6. As a consequence, pulsars show a narrow range of P and \dot{P} after evolution, which is not preferable by the observations. We also note that pulsars evolve much slower in this model.

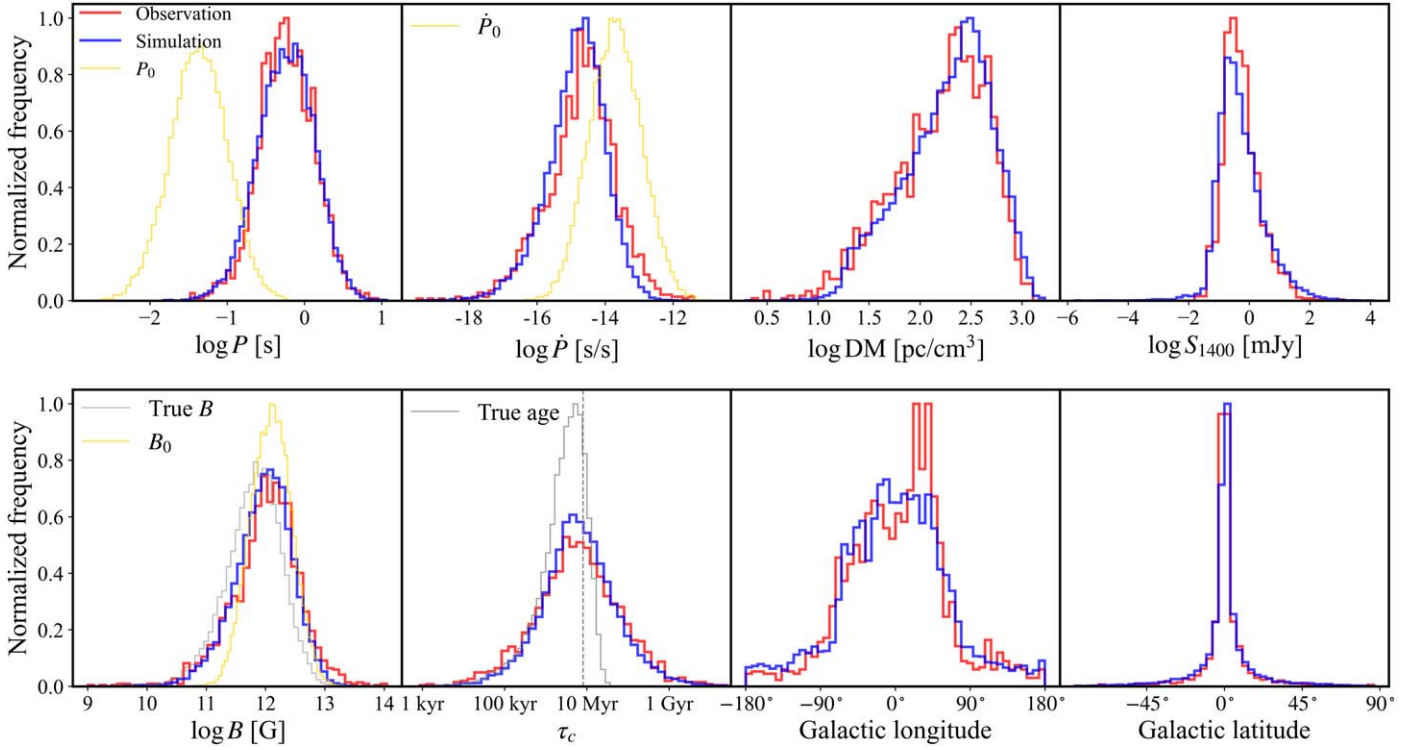


Figure 2. Distributions of observables for the simulated (blue) and observed (red) pulsar populations. The simulation is based on the exponential B -field decay model with the best-fit parameters. The initial spin period (P_0), initial spin-down rate (\dot{P}_0), and birth magnetic field strength (B_0) distributions (yellow histograms) are also shown for comparison. The magnetic field distributions shown by the red and blue lines are B_{SD} from Equation (37), and the true B -field from the simulations is plotted in gray color. The characteristic age τ_c is calculated with $P/2\dot{P}$, and the gray line shows the true age from simulations. The vertical dashed line in the plot indicates the best-fit ohmic decay timescale of 8.3 Myr.

Table 2
Best-fit Parameters with 1σ Confidence Intervals for the Exponential and Power-law B -field Decay Models

μ_P	σ_P	μ_B	σ_B	$\log \tau_{Ohm}$ (Myr)	α_B	$\log f_B$	$\log f_\nu$	α_ν	β_ν	D_{KS}
Exponential Decay										
$-1.40^{+0.48}_{-1.30}$	$0.35^{+0.84}_{-0.35}$	$12.32^{+0.05}_{-0.07}$	0.35 ± 0.03	$0.92^{+0.17}_{-0.20}$	$1.1^{+1.2}_{-0.8}$	$-1.76^{+0.28}_{-0.40}$	$0.67^{+0.10}_{-0.06}$	0.080
Power-law Decay										
$-1.62^{+0.3}_{-0.6}$	$0.36^{+0.41}_{-0.18}$	$12.33^{+0.04}_{-0.07}$	$0.35^{+0.04}_{-0.05}$...	$0.02^{+0.08}_{-0.02}$	$-15.6^{+0.3}_{-0.7}$	$0.9^{+0.3}_{-0.2}$	$-1.45^{+0.08}_{-0.18}$	$0.68^{+0.07}_{-0.05}$	0.082

In addition to the B -field strength, the inclination angle α between the magnetic and spin axes is another key factor that determines \dot{P} . Its evolution is plotted in Figure 6. It is clear that the evolution depends critically on B_0 . α drops rapidly for a large B_0 case, but it takes a long time to evolve if B_0 is low. This is expected, as $\dot{\alpha} \propto -B^2$ (see Equation (11)). At later times, α stops evolving when the B -field decays to very small values. In the exponential decay scenario, this happens when the evolution time exceeds τ_{Ohm} . The final value of α therefore remains relatively large for pulsars started with low B_0 . This effect, on the other hand, is less prominent for the power-law decay model. It can give a significantly smaller α for old pulsars, since the B -field stays comparatively larger until the end of the evolution.

In Figure 7, we plot the change of α for the simulated pulsars that are detected by the surveys. The pulsars are assumed to have isotropic α distribution at birth, but those with larger initial α (i.e., orthogonal rotators) have a higher chance of being detected. This is mainly due to the geometrical effect as

the emission beams of these pulsars are more likely to sweep across the Earth. Moreover, the plot also clearly illustrates the effect of α decay, which makes most of the detected pulsars become nearly aligned rotators ($\sim 18\%$ with $\alpha < 10^\circ$) at the end of the evolution.

In Figure 8, we plot the observed α versus characteristic age for 80 pulsars reported by Malov & Nikitina (2011) and compare with our best-fit model. The observations are generally consistent our model prediction, although not many pulsars are found in the most likely parameter space suggested by the model. We attribute the discrepancy to a small sample size and also the different beam geometry we adopt (core and cone beam) than the one (cone beam) assumed by Malov & Nikitina (2011) to deduce α .

3.5. Gamma-Ray Pulsar

After a pulsar is simulated, we calculated its phase-averaged gamma-ray flux according to the equations in Section 2.4.2. The result is then compared with the 14 yr Fermi all-sky

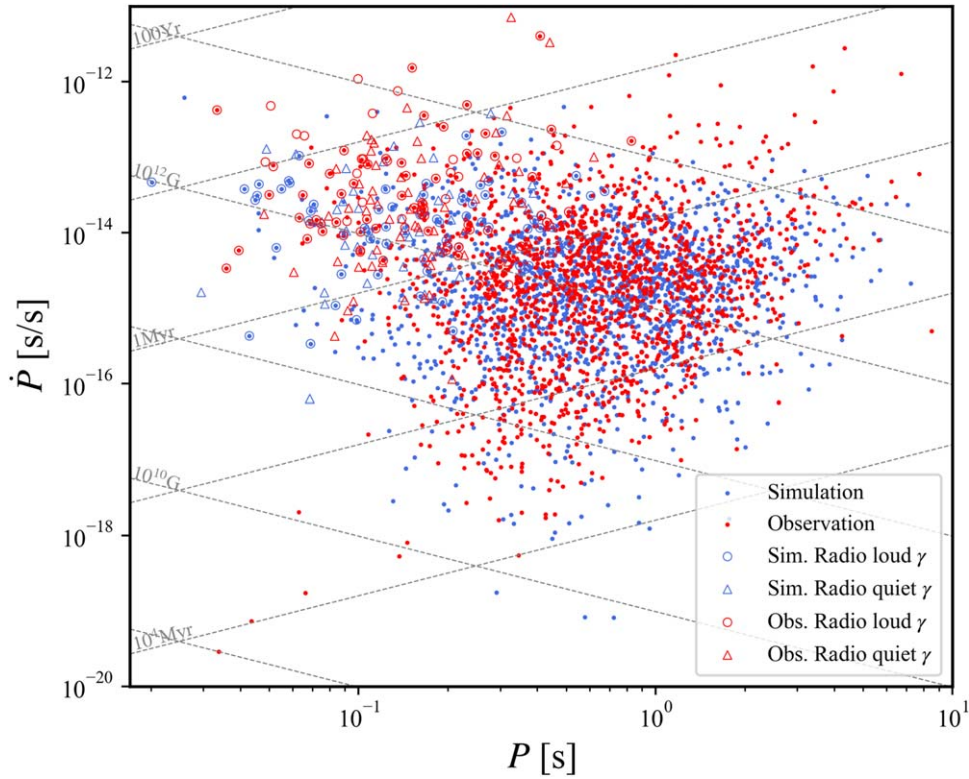


Figure 3. P – \dot{P} diagram for the observed (red) and simulated (blue) pulsars. The simulation is based on the exponential B -field decay model with the best-fit parameters. The red dots show the pulsar sample from radio surveys listed in Table 6. The red open circles and triangles show radio-loud and radio-quiet gamma-ray pulsars, respectively, from the third Fermi-LAT catalog (Smith et al. 2023).

sensitivity map² (Smith et al. 2023) to determine if it is visible. Table 3 lists the number of detectable radio-quiet and radio-loud gamma-ray pulsars based on the OG and TPC models, averaged from 100 simulations. We find that the OG performs better than the TPC. It can produce the number of radio-loud gamma-ray pulsars as observed in the third Fermi-LAT catalog (Smith et al. 2023), while the TPC model predicts too many. Figure 3 shows a random simulation of gamma-ray pulsars in the P – \dot{P} diagram using the preferred OG model. They occupy the same parameter space as the observed pulsars; both are in the upper left of the diagram, where \dot{E} is high.

4. Discussion

4.1. Magnetic Field Decay Model

In this paper, we present a detailed population study of normal pulsars using realistic physics inputs, including an updated spin-down formula, evolution of magnetic field strength and inclination angle, and sophisticated radio beam geometry. We fit the model to a large sample of pulsars using a rigorous statistical test and determine the optimal model parameters using MCMC. We parameterize the B -field evolution with the general form $dB/dt \propto B^{(1+\alpha_B)}$, and the best-fit result indicates that $\alpha_B = 0$ is preferred. This implies that the exponential decay model can better reproduce the observed pulsar population than the power law. We are able to constrain the decay timescale to be 8.3 Myr (1σ confidence interval of 5.2–12.3 Myr). This is comparable to the mean age of 4.8 Myr among the detected pulsars in the simulation, implying that B -field decay is nonnegligible in most pulsars.

It was suggested that ohmic dissipation in the crust due to phonon scattering is the primary cause of the magnetic field decay in normal pulsars (Igoshev & Popov 2015), and the Hall effect is only important for B -fields stronger than 10^{14} G (Viganò et al. 2013), which is much higher than that in our simulated pulsars (mean $\log B_0 = 12.3$ G). In this picture, the B -field would show a rapid decay at first driven by the Hall cascade. The ohmic decay then takes over at later times. This could help explain why the exponential model is preferred, as our result shows. The ohmic decay timescale τ_{Ohm} depends sensitively on a few physical parameters, including the temperature, impurity factor, and electron fraction (Igoshev et al. 2021). Using $T = 3.0 \times 10^8$ K and the typical values for other parameters, we can obtain $\tau_{\text{Ohm}} = 8.3$ Myr as our best-fit value.

4.2. Comparison with Previous Studies

Magnetic field decay has been considered in a number of pulsar population synthesis studies. These works adopt different models with various decay timescales ranging from 1 kyr to 10 Myr (e.g., Dirson et al. 2022; Xu et al. 2023; Graber et al. 2024). There was only one attempt to constrain the timescale directly from fitting, and a timescale $\tau = 4.3 \pm 0.4$ Myr was suggested for the exponential decay model (Cieřlar et al. 2020). While this is compatible with our result, we caution that they employ a simple spin-down formula without α evolution, and their pulsar sample is much smaller than ours. More importantly, they smoothed the observed pulsar distribution for model comparison, which may not accurately capture the statistic (see Graber et al. 2024).

² https://fermi.gsfc.nasa.gov/ssc/data/access/lat/3rd_PSR_catalog/

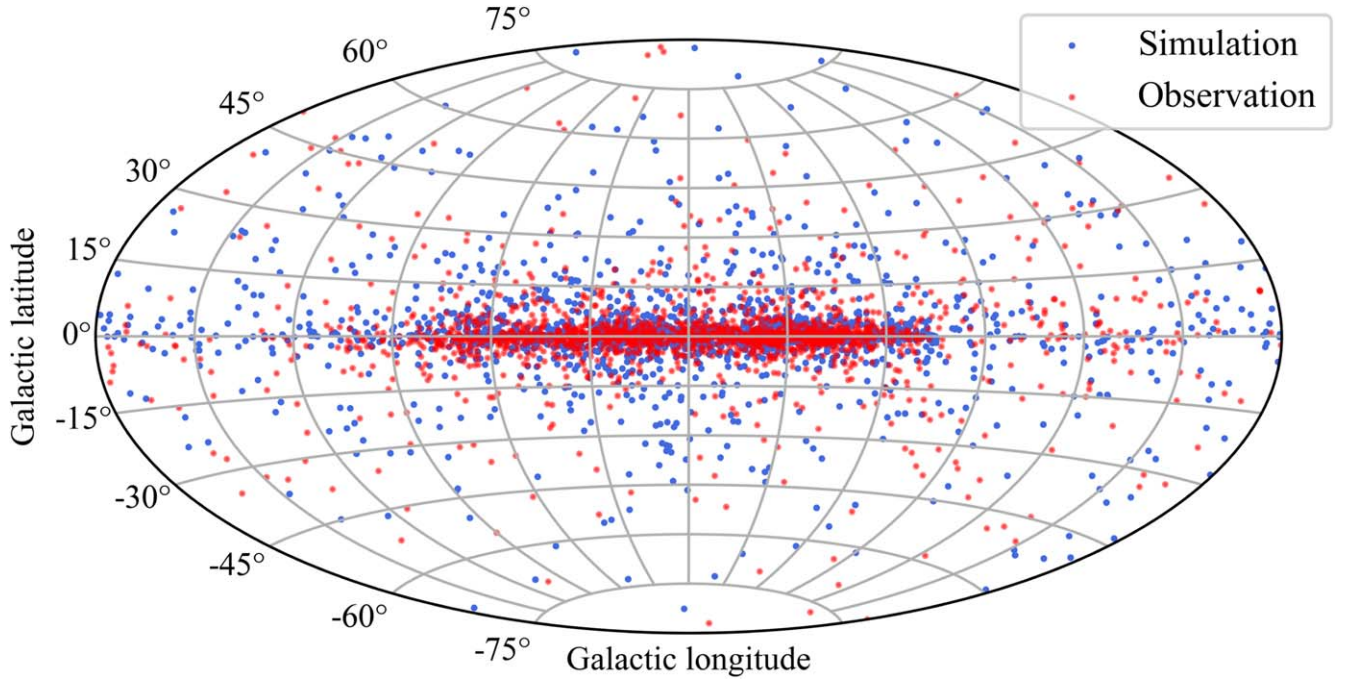


Figure 4. Galactic location distributions for the simulated (blue) and observed (red) pulsar populations. The simulation is based on the exponential B -field decay model with the best-fit parameters.

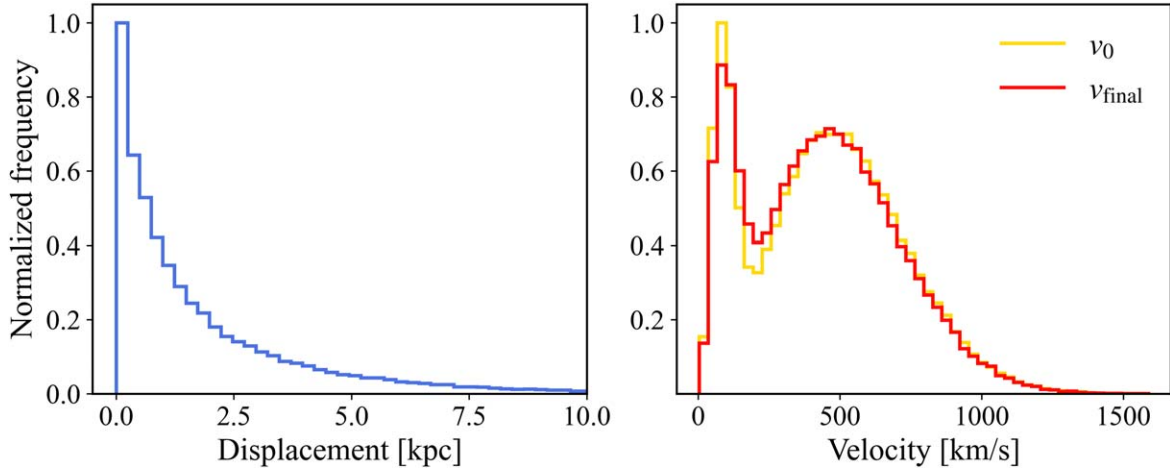


Figure 5. Dynamical evolution of simulated pulsars that are detected by the surveys. Left: distribution of pulsar displacement between their birth sites and final locations. Right: distribution of initial and final pulsar velocities at the end of the simulation.

The different decay timescales in previous studies could have an impact on the initial B -field required. Our best-fit model prefers a slightly lower B_0 with $\mu_B = 12.3$. This could be attributed to the strong correlation between μ_B and τ_{Ohm} , as Figure 1 shows. Our relatively long timescale suggests a late onset of the B -field decay, such that the initial field could be lower. The situation could be more complicated for the power-law model, since the decay timescale would depend on B_0 (see Dirson et al. 2022; Xu et al. 2023) instead of being fixed as assumed in some works (e.g., Graber et al. 2024).

Overall, all the population models for normal pulsars do not require strong B_0 ($\mu_B > 13.0$) even with the consideration of field decay. Our best-fit model produces only 0.2% of pulsars with $B_0 > 10^{13}$ G and none above 10^{14} G. This is not sufficient to explain magnetars, which have field strengths of 10^{14} – 10^{15} G (Kaspi & Beloborodov 2017). This suggests that this

class of objects could be a distinct population born with another channel.

The evolution of the magnetic inclination angle was studied in a recent work (Dirson et al. 2022), but a slightly different model was adopted for which the decay rate is independent of the B -field strength. Similar to our result, it was also found that the effect of α decay is significant, making the majority of pulsars nearly aligned rotators at the end of the evolution. However, their detected pulsars consist of mainly orthogonal rotators, which is contrary to our result. The discrepancy could be due to different radiation beam models. In particular, our core and cone emission components with Gaussian profiles allow detection even with very small alignment angles.

For the birth spin period distribution, our fit requires similar μ_P ($\mu_P = -1.40$) as in other studies, even using the updated sample (see Figure 3). However, we note that μ_P is not very

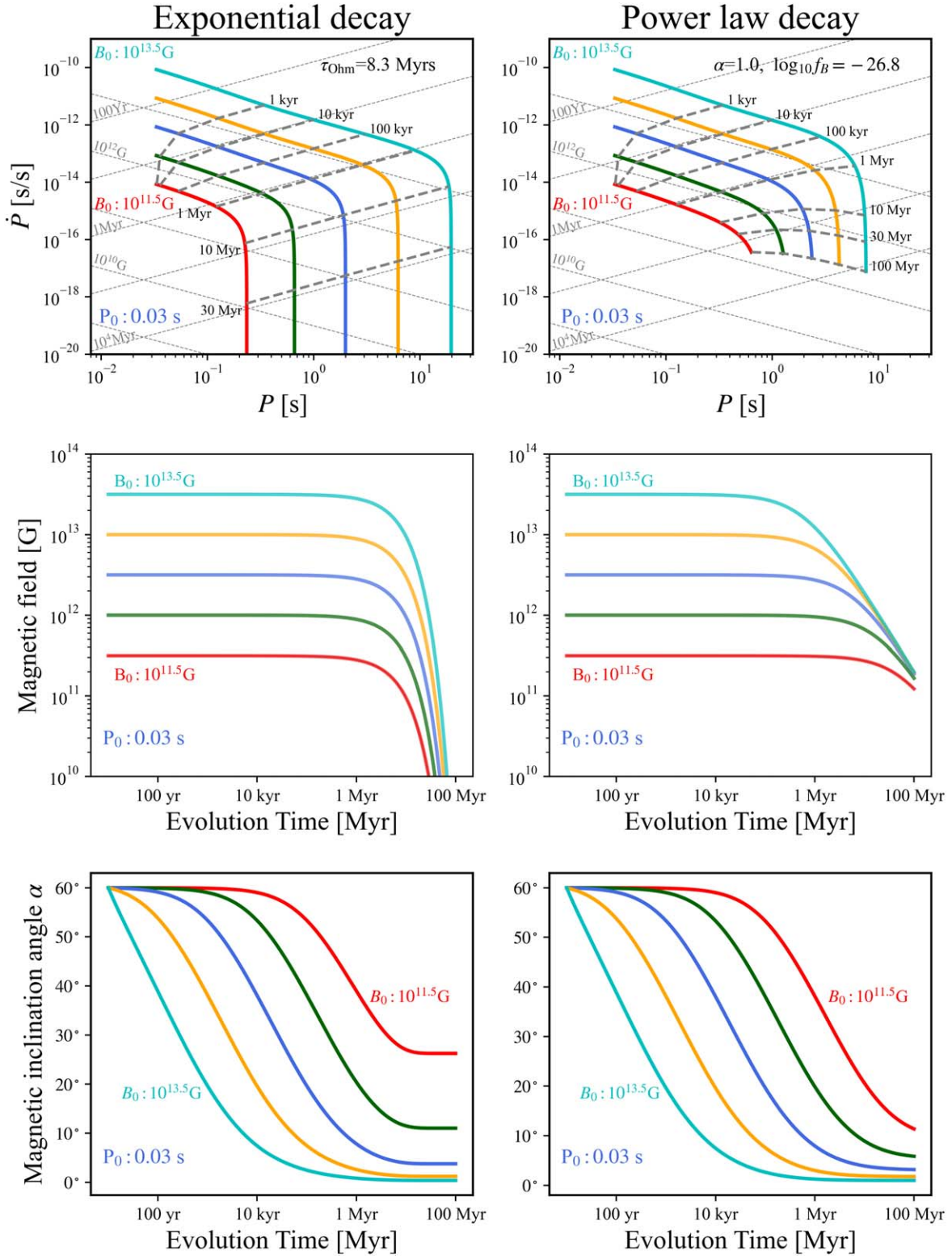


Figure 6. Pulsar evolution tracks in the P – \dot{P} diagram and the evolution of the magnetic field and the magnetic inclination angle (α) for the best-fit exponential B -field decay model. All pulsars start with $P_0 = 0.03$ s and initial $\alpha = 60^\circ$. Different colored lines represent different B_0 from 10^{11.5} G to 10^{13.5} G, uniform in logarithmic space.

well constrained in the fitting, and the large σ_P value suggests a broad distribution of P_0 . Such a result is consistent with the finding that the observed population is insensitive to the P_0 distribution and any values in the range of $P_0 < 0.5$ s could fit well (Gonthier et al. 2004; Gullón et al. 2014).

We parameterize the radio luminosity with the general form $L_\nu \propto P^{\alpha_\nu} \dot{P}^{\beta_\nu}$ as in previous studies. The best-fit result we found, $(\alpha_\nu, \beta_\nu) = (-1.76, 0.67)$, is close to the typically reported value of $(-1.5, 0.5)$; e.g., Faucher-Giguere & Kaspi 2006; Bates et al. 2014). Our slightly steeper dependence

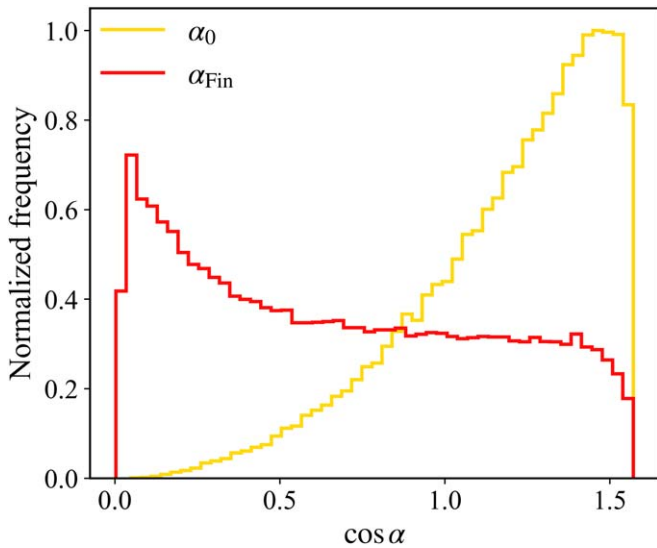


Figure 7. Distributions of the initial and final values (yellow and red lines, respectively) of the magnetic inclination angle α for the simulated pulsars detected with the surveys.

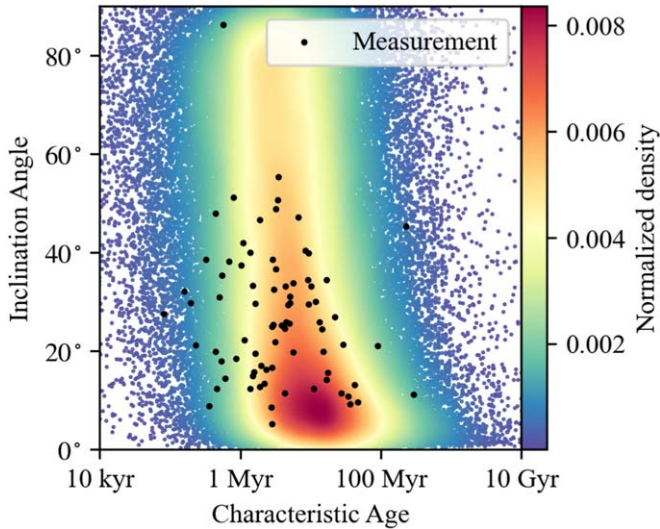


Figure 8. Magnetic inclination angle α vs. characteristic age for observed and simulated pulsars. The black dots show 80 measurements of α reported by Malov & Nikitina (2011). The underlying density plot is obtained by simulations of 50 times the pulsar sample (i.e., 92,950 pulsars) using our best-fit population model.

on P and \dot{P} could be attributed to the B -field decay, which results in more aged pulsars in the lower part of the P – \dot{P} diagram than in previous works. A larger β_ν is therefore needed to make them nondetectable, in order to match the observations. This also leads to a more negative value of α_ν due to the strong correlation between α_ν and β_ν (see Figure 1). We note that a very shallow dependence ($-0.39, 0.14$) was recently reported based on the MeerKAT Survey (Posselt et al. 2023). This, however, is not seen in other surveys (e.g., Anumalapudi et al. 2023), and more observations are needed to confirm this.

Alternatively, some studies investigate the correlations between L_ν and \dot{E} (e.g., Szary et al. 2014; Wu et al. 2020). We did not attempt to express L_ν in terms of \dot{E} in our modeling, since this requires a ratio, $R_{\alpha\beta} \equiv -\alpha_\nu/\beta_\nu = 3$, not supported by our results. The values of $R_{\alpha\beta}$ reported in the literature always lie between 2 and 3 (e.g., Faucher-Giguere & Kaspi 2006;

Table 3

Number of Gamma-Ray Pulsars in the Third Fermi-LAT Pulsar Catalog (Smith et al. 2023) Compared with Our Simulation Results Assuming the OG and TPC Models (Watters et al. 2009)

	Radio-loud	Radio-quiet
Third Fermi-LAT catalog	80 (53.3%)	70 (39.0%)
OG model	81 (59.2%)	55 (40.8%)
TPC model	128 (69.1%)	57 (30.9%)

Ridley & Lorimer 2010; Bates et al. 2014; Johnston & Karastergiou 2017; Posselt et al. 2023), and the value $R_{\alpha\beta} = 2.6$ we obtain is consistent with this range. On the P – \dot{P} diagram, this ratio corresponds to the slope of constant L_ν lines, which can be regarded as observation-limit lines (see Wu et al. 2020). It is interesting that the pulsar emission death lines expected from theories also share similar slopes (see Abolmsov et al. 2024, and references therein). This could imply a deeper physical connection underneath. We stress, however, that it is highly nontrivial to infer the pulsar intrinsic luminosity from observations, as this requires detailed knowledge of the radio beam geometry, the magnetic inclination angle, and the viewing angle. All of these are difficult to obtain, and any uncertainties will blur the correlation between L_ν , P , and \dot{P} .

Our study shows that it is possible to reproduce the pulsar P – \dot{P} distribution without assuming a death line, the same conclusion as Gullón et al. (2014) and Graber et al. (2024). Our luminosity law makes aged pulsars fade away and naturally become undetected. This results in an observation-limit line, which has the same effect as a death line from an observational point of view. On the other hand, we are unable to rule out the death line either. We tried fitting with the classical death line (Bhattacharya et al. 1992), but there is not much change in the model parameters. This is because in our model, most pulsars are already too faint to detect before they reach the death line. We note that the details of the death line could depend on many physical parameters, including the B -field strength, the magnetic inclination α (Beskin & Litvinov 2022), and even the equation of state (Zhou et al. 2017). Testing these ideas is beyond the scope of this work.

4.3. Pulsar Birth Rate

Our best-fit population model gives a normal pulsar birth rate of ~ 0.68 century $^{-1}$ in the Galaxy. This value is not affected by the age cutoff of 100 Myr assumed in the simulation, since pulsars that old cannot be detected. The birth rate we found is lower than those in previous pulsar population studies, e.g., 2.8 century $^{-1}$ from Faucher-Giguere & Kaspi (2006), 1.4 century $^{-1}$ from Lorimer et al. (2006), and 1.6–2 century $^{-1}$ from Graber et al. (2024), but still much higher than 0.16 century $^{-1}$ from Cieřlar et al. (2020). Our result indeed better aligns with the recent Galactic core-collapse supernova rate estimate of 1.63 ± 0.46 (Rozwadowska et al. 2021). However, we stress that the birth rates inferred from population modeling depend critically on the radio luminosity law, for which many of the details (such as the beam geometry) are not fully understood and could be subject to large uncertainties as discussed above. Additionally, including different surveys in the observation sample could give different birth rates (see Graber et al. 2024). This could be caused by unreliable survey parameters (see Section 4.4 below).

Table 4
Prediction about the Detectable Number of Future Radio Surveys

Survey	N_{det}	N_{dis}
FAST CRAFTS	1128	392
FAST GPPS	804	418
SKA	4646	2882
SKA–Mid	2617	1073
MeerKAT TRAPUM	3604	1983
CHIME	1236	498

Note. N_{det} and N_{dis} are the number of detectable and newly discovered Galactic normal pulsars by the surveys.

4.4. Prediction for New Surveys

We employ our best-fit model to make predictions for several upcoming pulsar surveys: the Commensal Radio Astronomy FAST Survey (FAST CRAFTS; Nan et al. 2011; Li et al. 2018) with updated parameters (D. Li 2024, private communication), the FAST Galactic Plane Pulsar Snapshot survey (FAST GPPS; Han et al. 2021), the Square Kilometre Array survey (SKA and SKA–Mid; Kramer & Stappers 2015) with parameters listed in Chakraborty & Bagchi (2020) and Cieřlar et al. (2020), the MeerKAT TRAPUM survey (Ridolfi et al. 2021), and the Canadian Hydrogen Intensity Mapping Experiment Pulsar Survey (CHIME; Good et al. 2021). The expected number of detections is listed in Table 4. We note that these could be very different from the actual numbers, possibly due to inaccurate survey parameters. For instance, the Giant Metrewave Radio Telescope High-Resolution Southern Sky (ghrss) and Green Bank Northern Celestial Cap (gbncc) surveys were expected to discover 80 new normal pulsars and 130 new MSPs, respectively (Stovall et al. 2014; Bhattacharyya et al. 2016), but in the end only 22 and 57, respectively, were found.

5. Conclusion

We carry out a population synthesis study for normal radio pulsars employing the most updated model inputs, including lognormal distributions for P_0 and B_0 (Igoshev et al. 2022), the spin-down formula from force-free magnetohydrodynamic simulations with exact dependence on the magnetic inclination angle (Philippov et al. 2014), the double Maxwellian distribution for the kick velocity (Verbunt et al. 2017; Igoshev 2020), the free electron density model by Yao et al. (2017), the core and cone radio emission model (Gonthier et al. 2018), and the latest empirical relation for gamma-ray luminosity (Kalapotharakos et al. 2017, 2019, 2022). We compared our simulation results with a large pulsar sample that covers all major surveys and performed a fitting utilizing the MCMC approach with a 4D KS statistic to constrain the model parameters. Our main findings are as follows.

1. The observed pulsar population can be well reproduced with the exponential B -field decay model. This model also performs substantially better than the power-law decay in terms of goodness of fit. The power-law model can only provide a good fit when $\alpha_B = 0$, which reduces into the exponential form. The results suggest that the ohmic dissipation could play an important part in the B -field decay process in neutron stars.
2. Our fitting is able to constrain μ_B to be 12.3 G and the magnetic field decay timescale to be $8.3^{+3.9}_{-3.0}$ Myr for the

exponential model. This implies that the decay is nonnegligible for most pulsars.

3. Due to the evolution of the magnetic inclination angle, we expect a large fraction of pulsars to have a good alignment between the magnetic and spin axes.
4. Our best-fit radio luminosity law $L \propto P^{-1.76}\dot{P}^{0.67}$ can reproduce the pulsar P – \dot{P} distribution without the need for a death line. However, we note that the exact values of the indices are model-dependent, and the largest uncertainty is from the emission beam geometry.
5. Employing the OG emission model, our population model can well reproduce the number of gamma-ray pulsars observed in the Galaxy.

Our study shows that pulsar population synthesis can provide a powerful tool to probe the physics of neutron stars. In future works, more microphysics could be included, such as the evolution of B -field geometry and its dependence on temperature and even the equation of state. Also, comparing the simulations with a large observational sample from upcoming surveys will provide better constraints on the model parameters.

Acknowledgments

We thank Wynn C. G. Ho for the discussion and useful suggestions. We thank the referee for the constructive advice. We thank D. Li for providing us with the FAST GPPS survey information. Z.S. and C.-Y.N. are supported by a GRF grant of the Hong Kong Government under HKU 17303221.

Appendix A Comparison with Observations

Among the 1859 pulsars in our sample, only 1624 have flux density measurements at 1400 MHz in the ATNF catalog. In order to keep the other 235 pulsars, we estimate S_{1400} from the measurement at the closest frequency available assuming a power-law spectrum with a spectral

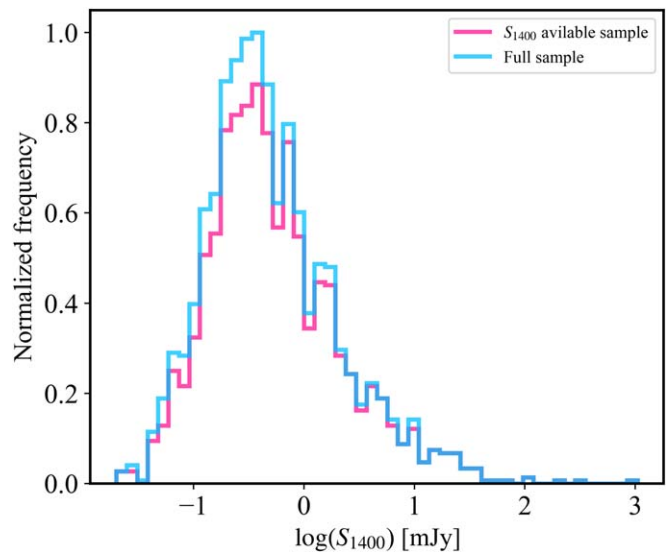


Figure 9. Distribution of radio flux density (S_{1400}) for 1624 pulsars with measurements from the ATNF pulsar catalog (red line) compared with the entire sample of 1859 pulsars (blue line). For pulsars that have measurements at other frequencies only, we scale their flux densities to 1400 MHz assuming a spectral index of -1.60 .

Table 5
Radio Surveys Not Used in This Work

Surveys Overlapped with Others	Surveys That Detected Fewer Than 25 Pulsars
ar2 (ar3 palfa lotaas)	ghrss (22)
ar327 (gbnce)	gbt350 (24)
gb1 (pksemb lotaas)	pksgnp (13)
gb4 (ar4 lotaas pksemb)	pkspa (14)
jb1 (ar3 pksemb lotaas)	pks_superb (23)
jb2 (palfa pksemb)	htru_eff (13)
mol1 (pks70 pkssw pksemb)	pksgc (0)
pks1 (pksemb)	tulipp (0)
fast_gpps (ar3 palfa pksemb)	mwa_smart (0)
	pumps (0)
	meerkat_trapum (0)

index of -1.60 . Figure 9 shows a comparison of the flux density distributions with and without these 235 pulsars. We apply the KS test and obtain a statistic of 0.0256 with p -value of 0.599, suggesting that using this S_{1400} estimate method has no significant effect on the distribution and hence should not affect our analysis results.

Table 5 lists the radio survey labels that are not used in this study, either fully overlapped by other surveys (the left column), or detected fewer than 25 normal pulsars according to our selection criteria mentioned in Section 2.6.1. Including all these surveys would only add 38 new pulsars to our sample. The parameters of radio surveys used in this work are listed in Table 6.

Table 6
Parameters of Radio Surveys Used in This Work

Parameters	ar1	ar3	ar4	palfa	gb2	gb3	gbncc	htru_pks	mol2	pkshl	pks70	pkssw	pksemb	lotaas
Degradation factor, β	1.0	1.0	1.0	1.0	1.0	1.0	1.3	1.0	1.0	3.0	1.5	1.5	1.5	1.0
Antenna gain (K Jy^{-1}), G_0	8–18	8–18	11	8.2	1.3	1.3	2.0	0.735	5.1	0.735	0.64	0.64	0.735	1.7
Integration time (s), t_{obs}	198	67.7	34	268, 134	136	132	120	4300, 540, 270	100	265	157.3	265	2100	3600
Sampling time (ms), τ_{samp}	5.6	0.516	0.506	0.064	16.7	2	0.08192	0.064	10	0.125	0.3	0.125	0.25	0.491
Receiver temperature (K), T_{rec}	90	50–75	120	24	30	30	46	23	210	21	50	21	21	360
Central frequency (MHz), f	430	430	429	1420	390	390	350	1352	408	1374	436	1374	1374	135.25
Bandwidth (MHz), ΔF	8	10	8	100, 300	16	8	100	340	4	288	32	288	288	31.64
Channel bandwidth (MHz), Δf	0.25	0.078	0.25	0.390, 0.293	2	0.25	0.0244	0.390	0.8	3	0.125	3	3	0.1953
Minimum R.A. (deg)	0	0	0	0	0	0	0	0	0	0	0	0	0	0
Maximum R.A. (deg)	360	360	360	360	360	360	360	360	360	360	360	360	360	360
Minimum decl. (deg)	−90	−1	0 ^a	−1	−18	−80	−40	−90	−85	−90	−90	−90	−90	−10
Maximum decl. (deg)	+90	+39	36 ^a	+38	+90	+65	+90	+90, +90, +10	+80	+90	0	+90	+90	+90
Minimum Galactic longitude (deg)	+35	+35	−180 ^a	+32, +170	−40 ^a	−180	−180	−80, −120, −180	−180	−140	−180	−100	−130	−180
Maximum Galactic longitude (deg)	+60	+80	+180 ^a	+77, +210	61 ^a	+180	+180	+30, +30, +180	+180	−100	+180	+50	+50	+180
Minimum Galactic latitude (deg)	−4	−8	−90	−5	−90	−20 ^a	0	−3.5, −15, −90	−18	−60	−90	−5	−6	−90
Maximum Galactic latitude (deg)	+4	+8	+90	+5	+90	+20 ^a	+90	+3.5, +15, +90	+18	+60	+90	+30	+6	+90
Detection SNR threshold, C	8.5	8.0	8.0	9.0	11.0	11.0	15.0	8.0	6.3	8.0	8.0	8.0	8.0	10.0

Note. The surveys and the corresponding references with survey parameters are as follows: Arecibo Survey 1 (ar1; Hulse & Taylor 1974, 1975), Arecibo Survey 3 (ar3; Fruchter et al. 1988; Nice et al. 1995), Arecibo Survey 4 (ar4; Wolszczan 1991; Thorsett et al. 1993; Lorimer et al. 2004), Arecibo Multibeam Survey (palfa; Cordes et al. 2006), Princeton-NRAO Survey (gb2; Dewey et al. 1985), Green Bank Short-Period Survey (gb3; Manchester et al. 1985), Green Bank North Celestial Cap Survey (gbncc; Stovall et al. 2014), High Time Resolution Survey-Parkes (htru_pks; Keith et al. 2010), 2nd Molonglo Survey (mol2; Manchester et al. 1978), Parkes High-Latitude Multibeam Pulsar Survey (pkshl; Manchester et al. 2001; Burgay et al. 2006), Parkes Southern Sky Survey (pks70; Manchester et al. 1996), Parkes-Swinburne Multibeam Survey (pkssw; Edwards et al. 2001), Parkes Multibeam Pulsar Survey (pksemb; Manchester et al. 2001), LOFAR Tied Array All-sky Survey (lotaas; Sanidas et al. 2019).

^a For some old surveys without a clear statement about the survey area in the literature, we estimate the region using their observed pulsar sample listed in the ATNF catalog.

Appendix B

Multivariate KS Statistic

After each simulation run, we need to compare the distributions of M simulated pulsars ($M = 10N$ in this study) and N observed pulsars ($N = 1859$ in our sample) for k observables (A, B, C, D, \dots) ($k = 4$ in our case). We evaluate the goodness of fit using the multivariate KS statistic (Fasano & Franceschini 1987; Justel et al. 1997), which is calculated as follows.

1. For each simulated or observed pulsar, call it the i th pulsar ($i = 1, \dots, N$ from observation or $i = 1, \dots, M$ from simulation), which has the properties ($A_i, B_i, C_i, D_i, \dots$). We first calculate the cumulative fraction of the observation sample compared with this i th pulsar (\mathcal{O}_i): if n observation pulsars satisfy the criterion ($A < A_i, B < B_i, C < C_i, D < D_i, \dots$), then

$$\mathcal{O}_{i,1} \equiv \frac{n}{N}. \quad (\text{B1})$$

There are totally 2^k different values of \mathcal{O}_i : $\mathcal{O}_{i,1}(A < A_i, B < B_i, C < C_i, D < D_i, \dots)$, $\mathcal{O}_{i,2}(A < A_i, B > B_i, C < C_i, D < D_i, \dots)$, ..., $\mathcal{O}_{i,2^k}(A > A_i, B > B_i, C > C_i, D > D_i, \dots)$ accounting for all the different definitions of \mathcal{O}_i , and $0 \leq \mathcal{O}_i \leq 1$.

2. Repeat a similar step calculating the cumulative fraction of the simulation sample compared with the i th pulsar: if m simulation pulsars satisfy the criterion ($A < A_i, B < B_i, C < C_i, D < D_i, \dots$), then

$$\mathcal{S}_{i,1} \equiv \frac{m}{M}. \quad (\text{B2})$$

Again, there are totally 2^k different values of \mathcal{S}_i : $\mathcal{S}_{i,1}(A < A_i, B < B_i, C < C_i, D < D_i, \dots)$, $\mathcal{S}_{i,2}(A < A_i, B > B_i, C < C_i, D < D_i, \dots)$, ..., $\mathcal{S}_{i,2^k}(A > A_i, B > B_i, C > C_i, D > D_i, \dots)$, and $0 \leq \mathcal{S}_i \leq 1$.

3. For this i th pulsar, calculate the maximum distance between $2^k \mathcal{O}_i$ and the corresponding $2^k \mathcal{S}_i$ as $D_i \equiv \max_{(j=1,2,\dots,2^k)} |\mathcal{O}_{i,j} - \mathcal{S}_{i,j}|$. If this i th pulsar is from observation, label the distance as $D_{\text{obs},i}$. If this i th pulsar is from simulation, label the distance as $D_{\text{sim},i}$.
4. Repeat (1)–(3) above to obtain the distance for each observed pulsar $D_{\text{obs},i}$ ($i = 1, 2, \dots, N$) and each simulated pulsar $D_{\text{sim},i}$ ($i = 1, 2, \dots, M$). Then calculate the maximum distance among the observed sample and the simulated sample, respectively: $D_{\text{obs,max}} \equiv \max(D_{\text{obs},1}, D_{\text{obs},2}, \dots, D_{\text{obs},N})$ and $D_{\text{sim,max}} \equiv \max(D_{\text{sim},1}, D_{\text{sim},2}, \dots, D_{\text{sim},M})$.
5. The KS statistic value is then $D_{\text{KS}} = (D_{\text{obs,max}} + D_{\text{sim,max}})/2$, with $0 \leq D_{\text{KS}} \leq 1$.

The value of D_{KS} indicates how well the simulated pulsar population matches that of the observed sample in terms of the observables, i.e., P, \dot{P} , DM, and S_{1400} in this work. The smaller the value, the better the match.

Since our simulation involves random sampling processes, this leads to fluctuation of the KS statistic; i.e., slightly different D_{KS} values are obtained every time, even with identical model parameters. To investigate this effect, we run simulations with the exponential decay model and the best-fit parameters and generate 1, 5, 10, 20, and 50 times more simulation pulsars than the observation sample. The whole process is repeated 100 times to determine the fluctuation in D_{KS} . The result is shown in Figure 10, and the 1σ (i.e., 68%) range and standard

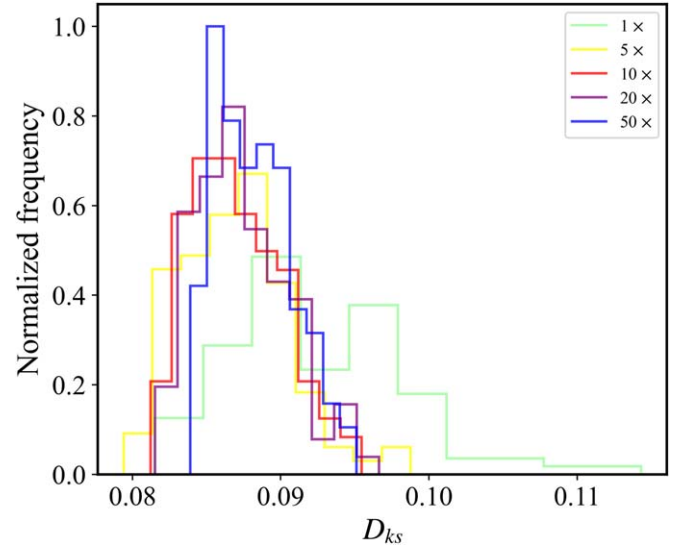


Figure 10. Fluctuation of KS statistic values for 100 simulations, all performed using the best-fit exponential decay model but with a different number of simulated pulsars 1, 3, 5, 10, 20, and 50 times more than the observation sample.

Table 7

1σ Range and Standard Deviation (SD) of the KS Statistic Obtained from 100 Simulations, Each with 1, 3, 5, 10, 20, and 50 Times More Simulated Pulsars Than the Observation Sample

No. of Sim. Pulsars	1σ Range	SD ($\times 10^{-3}$)
1 ×	0.0143	5.93
3 ×	0.0096	3.66
5 ×	0.0086	3.62
10 ×	0.0073	3.06
20 ×	0.0072	3.05
50 ×	0.0058	2.57

Note. All simulations are done with the exponential model using the best-fit parameters.

deviations are listed in Table 7. We find that simulating 10 times the number of pulsars as the observation sample (i.e., 18,590 simulations for 1859 pulsars observed) gives sufficiently small fluctuation of D_{KS} , and more simulations provide no significant improvement. Therefore, this is adopted in our simulation.

ORCID iDs

Zhihong Shi <https://orcid.org/0000-0002-1904-4957>
C.-Y. Ng <https://orcid.org/0000-0002-5847-2612>

References

- Abolmasov, P., Biryukov, A., & Popov, S. B. 2024, *Galax*, **12**, 7
Anumalapudi, A., Ehlke, A., Jones, M. L., et al. 2023, *ApJ*, **956**, 28
Arzoumanian, Z., Chernoff, D., & Cordes, J. 2002, *ApJ*, **568**, 289
Bates, S., Lorimer, D., Rane, A., & Swiggum, J. 2014, *MNRAS*, **439**, 2893
Belczynski, K., Benacquista, M., & Bulik, T. 2010, *ApJ*, **725**, 816
Beniamini, P., Hotokezaka, K., Van Der Horst, A., & Kouveliotou, C. 2019, *MNRAS*, **487**, 1426
Beskin, V., Gurevich, A., & Istomin, Y. N. 1988, *Ap&SS*, **146**, 205
Beskin, V., & Litvinov, P. 2022, *MNRAS*, **510**, 2572
Bhat, N. R., Cordes, J. M., Camilo, F., Nice, D. J., & Lorimer, D. R. 2004, *ApJ*, **605**, 759

- Bhattacharya, D., Wijers, R. A., Hartman, J. W., & Verbunt, F. 1992, *A&A*, **254**, 198
- Bhattacharyya, B., Cooper, S., Malenta, M., et al. 2016, *ApJ*, **817**, 130
- Bransgrove, A., Levin, Y., & Beloborodov, A. 2018, *MNRAS*, **473**, 2771
- Burgay, M., Joshi, B., D’Amico, N., et al. 2006, *MNRAS*, **368**, 283
- Chakraborty, A., & Bagchi, M. 2020, arXiv:2012.13243
- Cieslar, M., Bulik, T., & Osłowski, S. 2020, *MNRAS*, **492**, 4043
- Colpi, M., Geppert, U., & Page, D. 1999, *ApJ*, **529**, L29
- Cordes, J. M., Freire, P., Lorimer, D. R., et al. 2006, *ApJ*, **637**, 446
- Dewey, R., Taylor, J., Weisberg, J., & Stokes, G. 1985, *ApJ*, **294**, L25
- Dirson, L., Pétri, J., & Mitra, D. 2022, *A&A*, **667**, A82
- Edwards, R. T., Bailes, M., van Straten, W., & Britton, M. C. 2001, *MNRAS*, **326**, 358
- Fasano, G., & Franceschini, A. 1987, *MNRAS*, **225**, 155
- Faucher-Giguere, C.-A., & Kaspi, V. M. 2006, *ApJ*, **643**, 332
- Flowers, E., & Ruderman, M. A. 1977, *ApJ*, **215**, 302
- Foreman-Mackey, D., Hogg, D. W., Lang, D., & Goodman, J. 2013, *PASP*, **125**, 306
- Fruchter, A., Stinebring, D., & Taylor, J. 1988, *Natur*, **333**, 237
- Goldreich, P., & Reisenegger, A. 1992, *ApJ*, **395**, 250
- Gonthier, P., Story, S., Giachero, B., Arevalo, R., & Harding, A. 2006, *ChJAA*, **6**, 97
- Gonthier, P. L., Harding, A. K., Ferrara, E. C., et al. 2018, *ApJ*, **863**, 199
- Gonthier, P. L., Story, S. A., Clow, B. D., & Harding, A. K. 2007, *Ap&SS*, **309**, 245
- Gonthier, P. L., Van Guilder, R., & Harding, A. K. 2004, *ApJ*, **604**, 775
- Good, D., Andersen, B., Chawla, P., et al. 2021, *ApJ*, **922**, 43
- Graber, V., Ronchi, M., Pardo-Araujo, C., Rea, N., et al. 2024, *ApJ*, **968**, 16
- Gullón, M., Miralles, J. A., Viganò, D., & Pons, J. A. 2014, *MNRAS*, **443**, 1891
- Han, J., Wang, C., Wang, P., et al. 2021, *RAA*, **21**, 107
- Harding, A. K., Grenier, I. A., & Gonthier, P. L. 2007, *Ap&SS*, **309**, 221
- Haslam, C., Salter, C., Stoffel, H., & Wilson, W. 1982, *A&AS*, **47**, 1
- Hewish, A., Bell, S., Pilkington, J., Scott, P., & Collins, R. 1969, *Natur*, **224**, 472
- Hobbs, G., Lorimer, D., Lyne, A., & Kramer, M. 2005, *MNRAS*, **360**, 974
- Hulse, R., & Taylor, J. 1975, *ApJ*, **201**, L55
- Hulse, R. A., & Taylor, J. 1974, *ApJ*, **191**, L59
- Igoshev, A., & Popov, S. 2015, *AN*, **336**, 831
- Igoshev, A. P. 2019, *MNRAS*, **482**, 3415
- Igoshev, A. P. 2020, *MNRAS*, **494**, 3663
- Igoshev, A. P., Frantsuzova, A., Gourgouliatos, K. N., et al. 2022, *MNRAS*, **514**, 4606
- Igoshev, A. P., & Popov, S. B. 2020, *MNRAS*, **499**, 2826
- Igoshev, A. P., Popov, S. B., & Hollerbach, R. 2021, *Univ*, **7**, 351
- Jankowski, F., Van Straten, W., Keane, E., et al. 2018, *MNRAS*, **473**, 4436
- Jawor, J. A., & Tauris, T. M. 2022, *MNRAS*, **509**, 634
- Johnston, S., & Karastergiou, A. 2017, *MNRAS*, **467**, 3493
- Justel, A., Peña, D., & Zamar, R. 1997, *Statistics & Probability Letters*, **35**, 251
- Kalapotharakos, C., & Contopoulos, I. 2009, *A&A*, **496**, 495
- Kalapotharakos, C., Harding, A. K., Kazanas, D., & Brambilla, G. 2017, *ApJ*, **842**, 80
- Kalapotharakos, C., Harding, A. K., Kazanas, D., & Wadiasingh, Z. 2019, *ApJL*, **883**, L4
- Kalapotharakos, C., Wadiasingh, Z., Harding, A. K., & Kazanas, D. 2022, *ApJ*, **934**, 65
- Kaspi, V. M., & Beloborodov, A. M. 2017, *ARA&A*, **55**, 261
- Keith, M., Jameson, A., Van Straten, W., et al. 2010, *MNRAS*, **409**, 619
- Kijak, J., & Gil, J. 1998, *MNRAS*, **299**, 855
- Kijak, J., & Gil, J. 2003, *A&A*, **397**, 969
- Kramer, M., & Stappers, B. 2015, in Proc. of Advancing Astrophysics with the Square Kilometre Array (Trieste: Proceedings of Science), **36**
- Li, D., Wang, P., Qian, L., et al. 2018, *IMMAG*, **19**, 112
- Lorimer, D., Bailes, M., Dewey, R., & Harrison, P. 1993, *MNRAS*, **263**, 403
- Lorimer, D., Faulkner, A., Lyne, A., et al. 2006, *MNRAS*, **372**, 777
- Lorimer, D., McLaughlin, M., Arzoumanian, Z., et al. 2004, *MNRAS*, **347**, L21
- Malov, I., & Nikitina, E. 2011, *ARep*, **55**, 19
- Manchester, R., Amico, N. D., & Tuohy, I. 1985, *MNRAS*, **212**, 975
- Manchester, R., Lyne, A., Taylor, J., et al. 1978, *MNRAS*, **185**, 409
- Manchester, R. N., Hobbs, G. B., Teoh, A., & Hobbs, M. 2005, *AJ*, **129**, 1993
- Manchester, R. N., Lyne, A., d’Amico, N., et al. 1996, *MNRAS*, **279**, 1235
- Manchester, R. N., Lyne, A. G., Camilo, F., et al. 2001, *MNRAS*, **328**, 17
- Miyamoto, M., & Nagai, R. 1975, *PASJ*, **27**, 533
- Nan, R., Li, D., Jin, C., et al. 2011, *IJMPD*, **20**, 989
- Ng, C.-Y., & Romani, R. W. 2007, *ApJ*, **660**, 1357
- Nice, D., Fruchter, A., & Taylor, J. 1995, *ApJ*, **449**, 156
- Paczynski, B. 1990, *ApJ*, **348**, 485
- Pethick, C., & Sahriling, M. 1995, *ApJ*, **453**, L29
- Pétri, J. 2012, *MNRAS*, **424**, 605
- Philippov, A., Tchekhovskoy, A., & Li, J. G. 2014, *MNRAS*, **441**, 1879
- Popov, S., Pons, J., Miralles, J., Boldin, P., & Posselt, B. 2010, *MNRAS*, **401**, 2675
- Posselt, B., Karastergiou, A., Johnston, S., et al. 2023, *MNRAS*, **520**, 4582
- Rankin, J. M. 1993, *ApJ*, **405**, 285
- Ridley, J. P., & Lorimer, D. R. 2010, *MNRAS*, **404**, 1081
- Ridolfi, A., Gautam, T., Freire, P., et al. 2021, *MNRAS*, **504**, 1407
- Rozwadowska, K., Vissani, F., & Cappellaro, E. 2021, *NewA*, **83**, 101498
- Sanidas, S., Cooper, S., Bassa, C., et al. 2019, *A&A*, **626**, A104
- Smith, D. A., Abdollahi, S., Ajello, M., et al. 2023, *ApJ*, **958**, 191
- Spitkovsky, A. 2006, *ApJ*, **648**, L51
- Stovall, K., Lynch, R., Ransom, S., et al. 2014, *ApJ*, **791**, 67
- Szary, A., Zhang, B., Melikidze, G. I., Gil, J., & Xu, R.-X. 2014, *ApJ*, **784**, 59
- Tchekhovskoy, A., Spitkovsky, A., & Li, J. G. 2013, *MNRAS: Letters*, **435**, L1
- Thorsett, S., Deich, W., Kulkarni, S., Navarro, J., & Vasisht, G. 1993, *ApJ*, **416**, 182
- Verbunt, F., Igoshev, A., & Cator, E. 2017, *A&A*, **608**, A57
- Viganò, D., Rea, N., Pons, J. A., et al. 2013, *MNRAS*, **434**, 123
- Wainscoat, R. J., Cohen, M., Volk, K., Walker, H. J., & Schwartz, D. E. 1992, *ApJS*, **83**, 111
- Watters, K. P., Romani, R. W., Weltevrede, P., & Johnston, S. 2009, *ApJ*, **695**, 1289
- Weltevrede, P., & Johnston, S. 2008, *MNRAS*, **387**, 1755
- Wolszczan, A. 1991, *Natur*, **350**, 688
- Wu, Q.-D., Zhi, Q.-J., Zhang, C.-M., Wang, D.-H., & Ye, C.-Q. 2020, *RAA*, **20**, 188
- Xu, K., Yang, H.-R., Mao, Y.-H., et al. 2023, *ApJ*, **947**, 76
- Yao, J., Manchester, R., & Wang, N. 2017, *ApJ*, **835**, 29
- Yusifov, I., & Küçük, I. 2004, *A&A*, **422**, 545
- Zhang, C. M., & Kojima, Y. 2006, *MNRAS*, **366**, 137
- Zhou, X., Tong, H., Zhu, C., & Wang, N. 2017, *MNRAS*, **472**, 2403